Proceedings of IMECE2007
2007 ASME International Mechanical Engineering Congress and Exposition
November 11-15, 2007, Seattle, Washington, USA

IMECE2007-43115

A MICROGYRO WITH QUARTZ FORK SENSOR

Frank Wang
Systron Donner Automotive
2700 Systron Drive, Concord, CA 94518

ABSTRACT

Mainly targeting the automotive application, Systron Donner's MicroGyro with quartz fork sensor uses a vibrating quartz tuning fork to sense angular rate, acting as a Coriolis sensor, coupled to a similar fork as a pickup to produce the rate output signal. In this paper, the theoretical analysis of the quartz fork model is presented. Following that, the control of the drive magnitude and design of the pickup path are discussed in details. Experiment results from mechanical testing and electrical testing are presented to show that the MicroGyro has achieved 0.03°/s/rtHz.

INTRODUCTION

Gyroscopes are widely used in applications that require the measurement of angular rate. Gyroscopes find application in the automotive sector for rollover sensors, intelligent cruise control and vehicle dynamics etc. Gyroscopes are also in consumer devices such as camera stabilization, and inertial navigation. The principle of a vibrating gyroscope is well known. A proof-mass is driven to move along an axis in the proof mass plane, e.g. *x*-axis. When it experiences a rotation about another axis, e.g. *z*-axis, a Coriolis force is generated in *y*-axis, which is perpendicular to both the driving direction *x*-axis, and the rotation direction *z*-axis. The angular rate is inferred through the detection of the motional change in *y*-axis of the proof-mass caused by the Coriolis force.

Many research efforts have gone into the micromachined gyroscope [1]. Current micromachined gyroscopes have been demonstrated both in open-loop sensing [2] and closed-loop sensing with digital feedback [3]. Closed-loop sensing has the potential to increase the sensor bandwidth, improve linearity, and reduce sensitivity to process and temperature variations. In certain applications, such as the field of aerospace & defense and automotive stability control, the scale factor of the sensor needs to be very accurate and stable. Thus a driving servo loop, namely AGC loop, is necessary to keep the vibration amplitude of the proof mass constant. The output of the sensing loop then becomes proportional only to the input angular rate and is not affected by the variation in the driving amplitude.

Systron Donner's MicroGyro with dual end fork, as shown in Fig. 1, uses a vibrating quartz tuning fork (drive tines) to sense rate, acting as a Coriolis sensor, coupled to a similar fork (pickup tines) as a pickup to produce the rate output signal. The sensor along with its support flexures and frames are batch fabricated from thin wafers of single-crystal piezoelectric quartz. The piezoelectric drive tines are driven by an oscillator at precise amplitude, causing the tines to move toward and away from one another in anti-phase motion at the drive resonant frequency. This vibration causes the drive fork to become sensitive to angular rate about an axis parallel to its tines, defining the true input axis of the sensor. For vibrating tines, an applied rotation rate causes a sine wave of torque to be produced, resulting from "Coriolis acceleration." This, in turn, causes the tines of the pickup fork to move up and down (not toward and away from one another) out of the plane of the fork assembly. The pickup tines thus respond to the oscillating torque by moving in and out of plane, producing electrical output signals. These signals are then amplified and converted into a base-band signal proportional to rate by use of a synchronous demodulator responding only to the desired rate signals. The base-band output signal of the MicroGyro is directly proportional to input rate, reversing sign as the input rate reverses, since the oscillating torque produced by Coriolis force reverses phase when the input rate reverses.

Fig. 2 shows the block diagram of the MicroGyro, and Fig.3 is the die layout. Main blocks include AGC/OSC drive loop, AFE, DAS monitoring and uC 8051 etc. The MicroGyro with a quartz rate sensing element detects and processes angular rate for stability and rollover automotive applications. This MicroGyro has the capability to provide serial digital output through SPI. The uC 8051 provides compensation for the angular rate signal over temperature, sub-circuit(s) failure detection, and SPI digital data communications through a firmware solution via the use of metal mask ROM, RAM, and programmable memory (Zenerzap memory). Additionally, the MicroGyro processes data from two external auxiliary channels, which can be connected with accelerometers or other sensors.

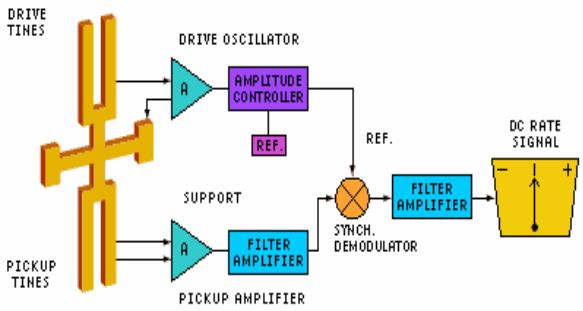

Figure 1. Operation Model of Systron Donner's MicroGyro

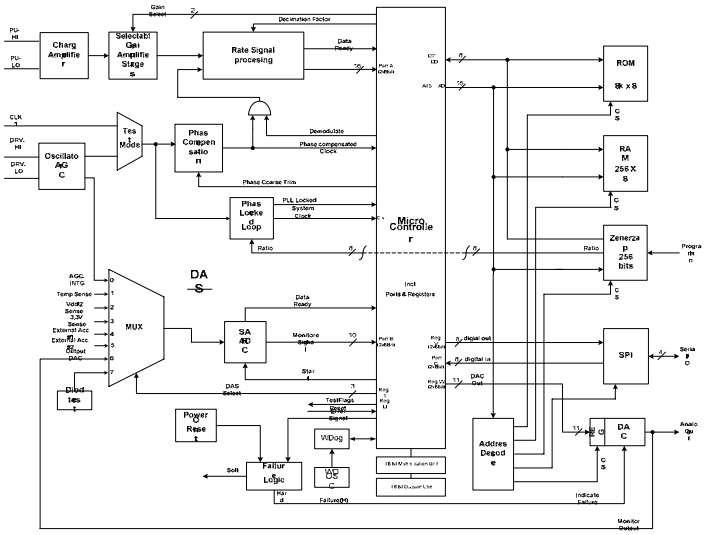

Figure 2. Systron Donner's MicroGyro Block Diagram

The modeling of the fork and analysis of the fork's dynamics help to understand and optimize the design of the fork. In this paper, the fork will be characterized in detail and the circuit design for both drive oscillation loop and the pickup path will be presented. The MicroGyro performance is summarized as follows:

Power supply: 5V, 35mA;
Temperature range: -40°C to +125°C;
Angular acceleration: 500°/s^2;
Physical dimension: 16x19x6 (mm);
Scale factor error: ±2%;
Linearity: ±0.5°/s;
Total offset error: ±1°/s;
Offset error due to temperature: ±0.5°/s;
Cross axis sensitivity: 3.5% of scale factor;
Frequency response: 35 / 65 / 80 / 120 Hz;
Output noise: 0.03(°/s)/rtHz;
Turn on time: 800mS nominal;
SPI data rate: 2MHz nominal;
SPI measuring range: ±300°/s;
SPI sensing saturation range: ±819°/s;
SPI resolution: 0.025°/s/LSB;
Analog rate out scale factor:
Ratiometric: 27mV/°/s for ±75°/s range;
20mV/°/s for ±100°/s range;
10mV/°/s for ±200°/s range;
6mV/°/s for ±300°/s range;
Non-ratiometric: 22mV/°/s for ±75°/s range;
16mV/°/s for ±100°/s range;
8mV/°/s for ±200°/s range;
5mV/°/s for ±300°/s range;

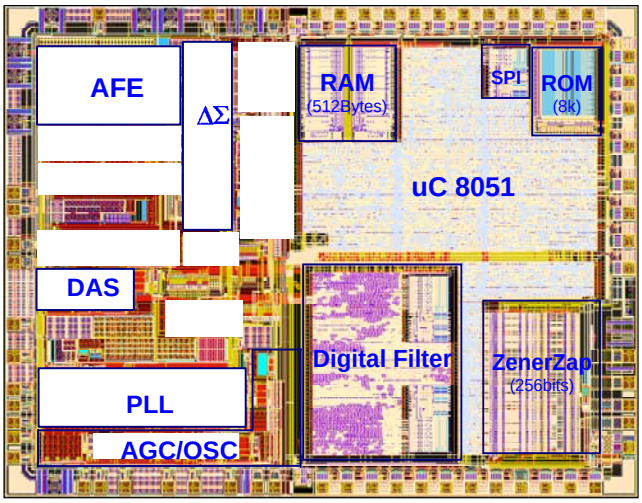

Figure 3. Systron Donner's MicroGyro Die Layout

QUARTZ FORK CHARACTERIZATION

The MicroGyro angular rate sensing concept is based on the Coriolis Effect. This physics effect, first described by Coriolis in 1835, is common to most MEMS rate sensing concepts today. An illustration of the Coriolis Effect is depicted in Figure 4. The figure represents an end view of a vibrating tuning fork.

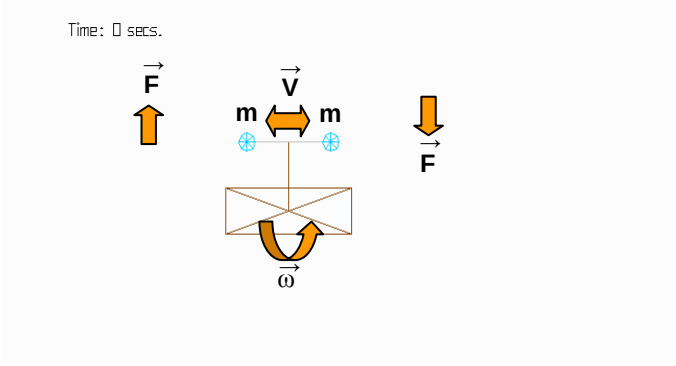

Figure 4. Coriolis Effect Demonstration

The identical tuning fork tines are oscillating in an anti-phase mode (equal and opposite motion) at a constant

frequency (f) determined by the mass and stiffness of the fork tines according to the following equation:

$$f \propto \sqrt{(k/m)} \tag{1}$$

where: f is resonant frequency, k is fork tine stiffness and m is fork tine mass

Typical MEMS gyro drive frequencies lie in the 5-20kHz region for most Coriolis effect devices. Systron Donner's MicroGyro applications occupy the 10-18kHz drive frequency range.

The Coriolis forces are perpendicular to both the tuning fork vibrating plane and the angular rate sensing axis. The Coriolis forces are equal and opposite on the two tines, due to their anti-phase motion. The two tine masses resist with force any change in orientation of the vibration plane as the fork is rotated in the sensing axis. As rotation rate increases, proportionately larger forces are generated.

The quart rate sensor has been in continuous development for over 20 years. Despite many variations, the common core architecture is fundamental to every embodiment of this Coriolis effect sensor.

The MicroGyro combines a classical crystal oscillator function with a design that generates forces proportionate to angular rate using the Coriolis acceleration-generated forces per equation 2:

$$\vec{F} = 2m\vec{V} \times \vec{\omega} \tag{2}$$

where m is tine mass, V is tine velocity and ω is the angular rate in sensing axis.

The quartz sensing element is stressed by the Coriolis forces and generates a charge proportionate to the stress, due to the piezoelectric property of the quartz. The force, F, is sinusoidal at the same frequency as the drive vibration, V. The charge is proportionate to the angular rate, ω, and is also sinusoidal at the same frequency. Sensitive circuits process the small charge, amplifying it and converting it from the drive frequency to base-band (near DC) by a synchronous demodulator and low-pass filter. The resulting near DC signal exhibits amplitude proportionate to angular rate and a polarity indicating direction of rotation.

The drive tines and pickup tines of the quartz fork sensor can be modeled respectively as an equivalent crystal element circuit as shown in Fig. 5. The elements are a resistor, a capacitor and an inductor in series (denoted R_s, C_s & L_s, respectively) with another capacitor (C_0) in parallel. The series elements are electrical equivalents, while the parallel capacitor is a real capacitor formed by the electrodes and leads.

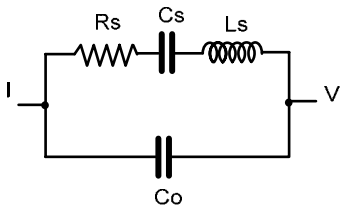

Figure 5. Simplified Lumped Element Fork Model

The network has both a series and parallel resonant frequencies that are typically separated by less than one percent. This equivalent circuit applies to a crystal operating at its fundamental resonant frequency. Some crystals are specified to operate on a 3rd or 5th overtone in which case one or two additional series resonant arms must be added to the equivalent circuit. Admittance of the series arm is

$$Y_s = \frac{1}{R_s + j\omega L_s + \frac{1}{j\omega C_s}} \tag{3}$$

With the admittance from the shunt capacitor, the network admittance can be expressed as

$$Y = Y_s + j\omega C_0 = \frac{1}{R_s + j\left(\omega L_s - \frac{1}{\omega C_s}\right)} + j\omega C_0 \tag{4}$$

The Q of these resonators usually lies between 12,000 and 20,000 and hence *Rs* has negligible effect on the resonant frequency and it has been ignored in the following resonant frequency equations. By definition the parallel (i.e. anti-) resonant frequency is that frequency at which the capacitive and inductive reactance cancels, leaving only the resistive component. This frequency is found by equating the complex term (above) to zero and solving for the resonant frequency. The equation has several solutions but only the following one yield a positive, non-zero frequency for positive component values:

$$\omega_p = \frac{\sqrt{C_s + C_0}}{\sqrt{C_0} \cdot \sqrt{L_s C_s}} \tag{5}$$

By definition the series resonant frequency is that frequency at which the capacitive and inductive reactance cancels, leaving only the resistive component. This frequency is found by equating the complex term (in the impedance equation above) to zero as follows,

$$\omega_s = \frac{1}{\sqrt{L_s C_s}} \tag{6}$$

So the ratio of the two frequencies is

$$\frac{\omega_p}{\omega_s} = \sqrt{1 + \frac{C_s}{C_0}} \tag{7}$$

For one QRS fork from Systron Donner, the drive tines have a drive frequency of 11.28kHz and Q of 15700. The lumped element parameters are R_s=260kΩ, L_s=56861H, C_s=3.5fF, and C_0=1.8pF. So the resonant frequency and anti-resonant frequency are

$$f_{res} = \frac{1}{2\pi}\sqrt{\frac{1}{56861\times 3.5\times 10^{-15}}} = 11.282\,(\text{kHz}) \quad (8)$$

$$f_{anti-res} = f_{res}\sqrt{\left(1+\frac{C_s}{C_0}\right)} = 11.293\,(\text{kHz}) \quad (9)$$

As shown in Fig. 6, the frequency response of this drive tine indicates the resonant frequency at 11.282kHz, and an associated anti-resonant frequency around 11.293kHz. More interesting, the phase experiences a 180 degrees shift (lag) and then another 180 degrees shift (lead). Fig.6 also shows the frequency responses with different C_0 values.

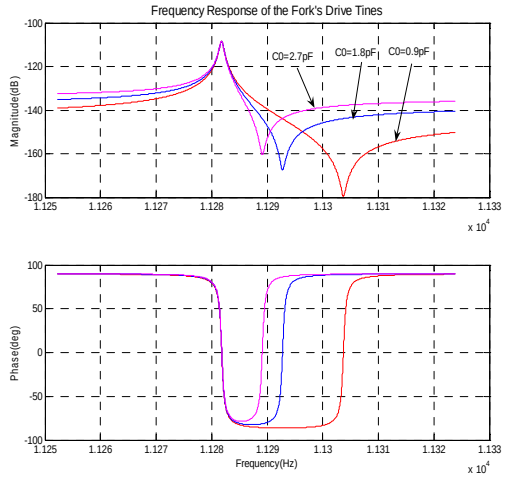

Figure 6. Frequency Response of the Drive Tines

Based on the above discussion, a transfer function model can be extracted from the fork as follows

$$H(s) = \frac{I}{V} = \frac{L_s C_s C_0 s^3 + R_s C_s C_0 s^2 + (C_s + C_0)s}{L_s C_s s^2 + R_s C_s s + 1} \quad (10)$$

Systron Donner's quartz fork sensor has many groups of forks according to different drive frequencies, different pickup frequencies and different Q's. The stronger sensitivities with the newer, smaller (and lower cost) forks represent a major advancement in the robustness of quartz tuning fork design.

Table 1 shows the comparison of the two fork families' sensitivity.

Table 1. Fork Sensitivity Comparison

Fork Model	Relative Size	Relative Sensitivity	Figure of Merit (sensitivity/size)
STD4	100	100	1.0
STD8	71	252	3.5

The STD8 achieved significant cost reduction for several reasons including more forks per wafer, lower process time in etch, and higher performance resulting in higher yields at final test. As with the STD4, the STD8 featured a center point mount which guaranteed that no thermal expansion stresses could affect fork operation/performance due to differences in mount material and quartz.

The tapered tine/hammerhead design offers higher sensitivity with a smaller fork size, a result opposite to that expected with a fork size reduction. This improvement is the result of both better drive behavior, and enhanced pickup coupling. The drive system has a higher "Q", due to reduced tine displacement and improved charge coupling of the tines. This lowers impedance allowing for higher drive current levels from a given voltage source, and decreases zero rate offset bias.

Finally, the tapered tine concept offers design control variables that include not only length and width (as with the square tine design), but also taper and hammerhead mass size. This additional design flexibility allows for more optimization of the overall structure, and eases challenges such as the pickup mode nodal line centering.

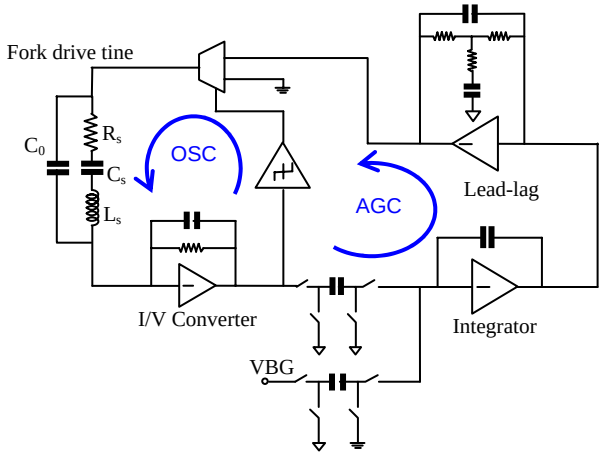

Figure 7. Block Diagram of the AGC/Oscillator Loop

AGC/OSC DRIVE LOOP

The AGC/Oscillator loop system is shown in Fig. 7. Basically it consists of two loops, namely an AGC loop and an oscillator loop. There are four main blocks in this system, the fork model, current to voltage converter (I/V), SC FWR/integrator, and lead-lag circuit. VBG is a reference voltage derived from a bandgap circuit.

1. SC FWR/integrator

In the AGC loop, in order to control the crystal current, the oscillator signal (about 11kHz in Systron Donner's QRS) needs to be full-wave-rectified to a DC value, integrated and then compared with a predefined reference voltage to set the AGC level. As shown in Fig. 8, the SC integrator block can realize all three functions: full-wave rectification, integration and summation. The summation is employed before the integrator.

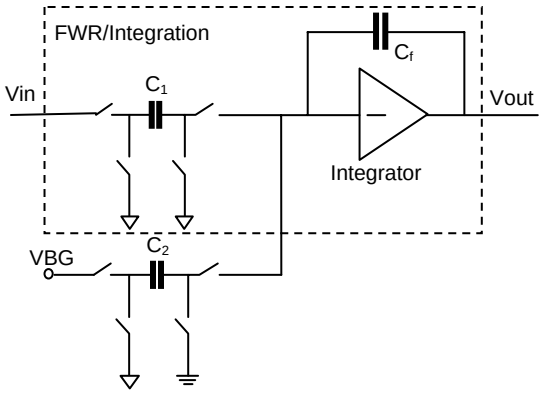

Figure 8. Block Diagram of the SC Integrator

The FWR and integration block, shown inside the dotted line area in Fig. 8, was simulated in Pspice with a frequency of 10kHz and 400mVpeak sinusoidal input. The switch clock frequency is 250kHz, the C1 capacitor value is 800fF, and the feedback has a capacitor of 20pF and resistor of 10MΩ . The result is shown in Fig. 9. The integrator output level is about 508mV, as expected.

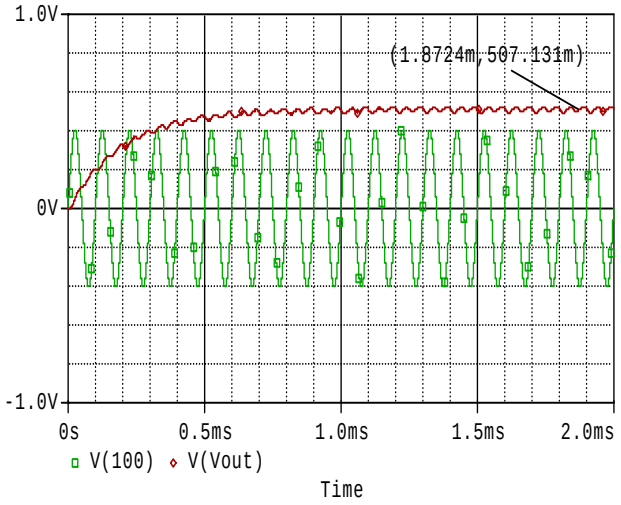

Figure 9. SC FWR Simulation Results

The SC block has an equivalent impedance given by

$$R_{eq} = \frac{1}{fC} \tag{11}$$

where *f* is the clock frequency for switch operation and C is the capacitance value of the capacitor.

So in the summation, there is a relationship between reference voltage VBG and Vin as in equation (12).

$$V_{in-peak} = \frac{C_2}{C_1} \cdot \frac{\pi}{2} V_{BG} \tag{12}$$

2. Stability: Lead-lag circuit

Lead and lag compensators are used quite extensively in control. A lead compensator can increase the stability or speed of response of a system; a lag compensator can reduce (but not eliminate) the steady state error. Depending on the effect desired, one or more lead and lag compensators may be used in various combinations.

A lead-lag compensator combines the effects of a lead compensator with those of a lag compensator. The result is a system with improved transient response, stability and steady-state error. To implement a lead-lag compensator, first design the lead compensator to achieve the desired transient response and stability, and then add on a lag compensator to improve the steady-state response.

The lead-lag circuit used in the AGC loop employs a T-network structure as shown in Fig. 10 with the transfer function in Eq. (21).

$$H_{ll}(s) = -\frac{1}{R_i} \frac{sC_z(R_1R_2 + R_1R_f + R_2R_f) + R_1 + R_f}{s^2C_fC_z(R_1R_2 + R_1R_f + R_2R_f) + s[C_z(R_2 + R_f) + C_f(R_1 + R_f)] + 1} \tag{13}$$

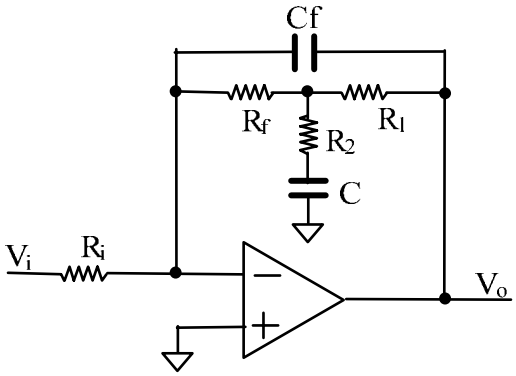

Figure 10. Lead Lag Circuit for Stability

With all parameters chosen appropriately, it has the following transfer function and the frequency response shown in Fig. 11.

$$H_{ll}(s) = \frac{-2.32 \times 10^{-2} s - 1}{1.230528 \times 10^{-6} s^2 + 3.25304 \times 10^{-3} s + 1} \tag{14}$$

This frequency response will give maximum of 47 degrees phase boost in the frequency range of interest of 30Hz to 200Hz to improve the transient response, stability and steady-state error of the AGC system.

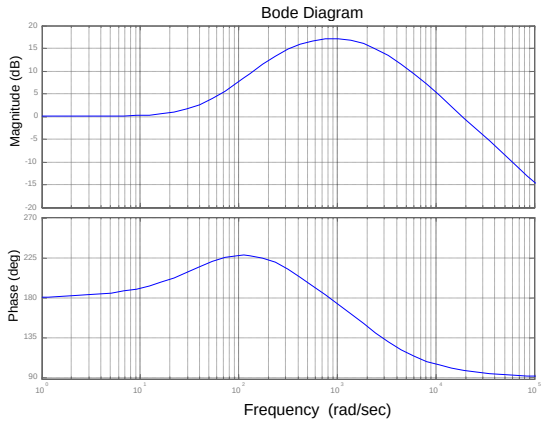

Figure 11. Frequency Response of the Lead-lag

3. System response

The AGC/Oscillator loop response is analyzed using Matlab Simulink. The Simulink model is shown in Fig. 12, which is directly generated from block diagram Fig. 3, including fork model, current to voltage converter (I/V), SC FWR/integrator, and lead-lag circuit.

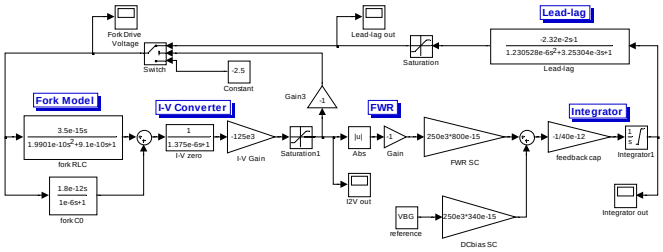

Figure 12. Matlab Simulink Model of AGC/OSC Loop

The fork model is

$$H_{fork}(s) = \frac{3.5\times10^{-15}\,s}{1.9901\times10^{-10}\,s^2 + 9.1\times10^{-10}\,s + 1} \quad (15)$$

The simulation results of this model are shown in Fig. 16. Fig. 13 (a) shows that fork's vibration has built up in about 400mS, so the I/V output voltage (proportional to crystal current) reaches the designed 0.8Vp value. Fig. 13 (b) is the integrator output. It shows that the integrator is saturated at the beginning, which corresponds to the full-scale drive voltage in the "DRH Voltage" as shown in (c). When the AGC input level reaches a certain threshold value, the oscillation magnitude is then controlled by the AGC loop. This configuration is designed for high magnitude drive at startup that drives the oscillation of the fork very hard at the beginning. The simulation results show the system is slightly under-damped, which help to shorten the turn-on time.

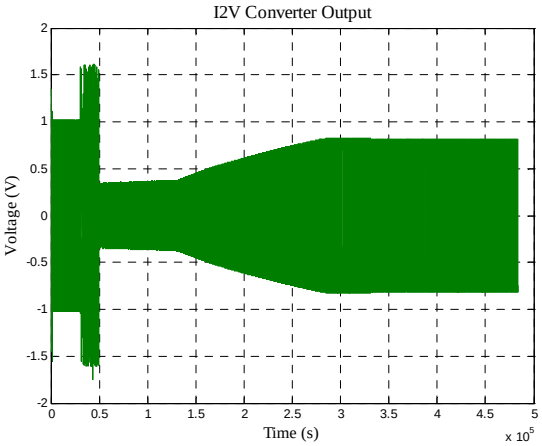

Figure 13. (a) I2V Converter Output

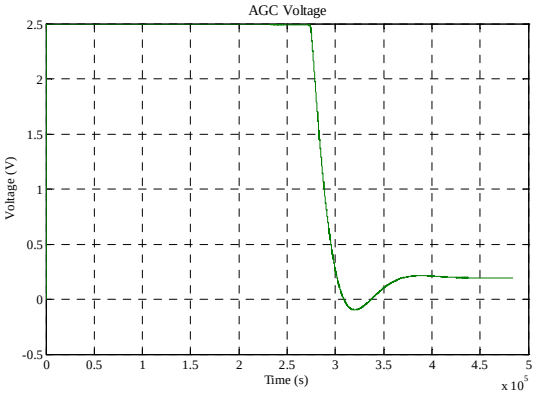

Figure 13. (b) AGC Integrator Output

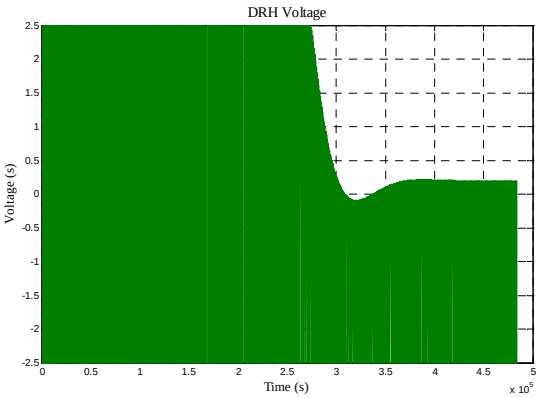

Figure 13. (c) Fork Drive Voltage

PICKUP SIGNAL PATH

The pickup signal path includes AFE (Analog Front End), delta sigma modulator, digital filter chain and uC 8051 for digital signal processing.

As discussed in previous section, the pickup tines produce a charge signal proportional to input angular rate. For example, one kind of fork with name STD8-D has a scale factor of

$$SF=18aCrms/(°/s)/uA \qquad (16)$$

which means the scale factor is proportional to drive crystal current. When the AGC/OSC provides a constant crystal current, the charge signal at pickup tines will represent the input angular rate.

The charge amplifier block is differential as shown in Fig. 14. Each charge amplifier consists of a LNA (low noise amplifier) with feedback capacitor and high impedance resistor. The charge amplifier transfers the charge from the pickup tines to voltage. The PGA has 4 adjustable gain settings.

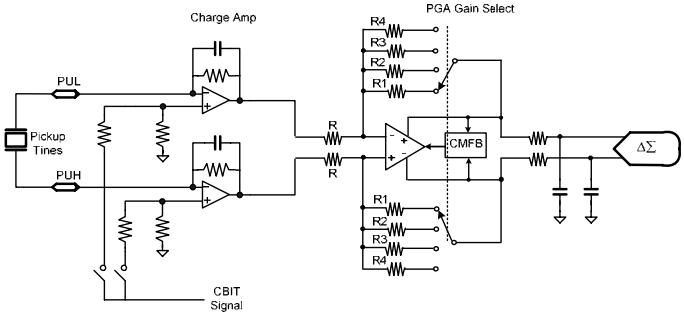

Figure 14. MicroGyro Analog Front End

With charge as input, the charge amplifiers has the following transfer function.

$$H(s)=\frac{V}{Q}=\frac{sR}{1+sRC} \qquad (17)$$

where R is the feedback resistor and C is the feedback capacitor. The requirements for the feedback resistor are:

- Discharge C_F
- Source I_{leak}
- Minimum noise
- Linear
- Insensitive to process, temperature and supply variance
- Low capacitance
- Resistance in the range of MΩ~GΩ

There are many ways to implement a high impedance resistor feedback for the charge amplifier. The well-known one is T-network resistor structure as shown in Fig.?? (a). The equivalent resistance is

$$R=\frac{R_2}{R_1}\bullet R_f \qquad (18)$$

The T-network is simple and easy to impelement, and can make large resistor. But it will show large parasitic capacitance, and it is not adjustable to I_{leak}. It also introduces noise from resistors.

The second approach is shown in Fig. 15 (b) with anti-parallel MOS diodes. And an improved version shown in (c), which can achieve 500MΩ, and it is adjustable by varying the bias current.

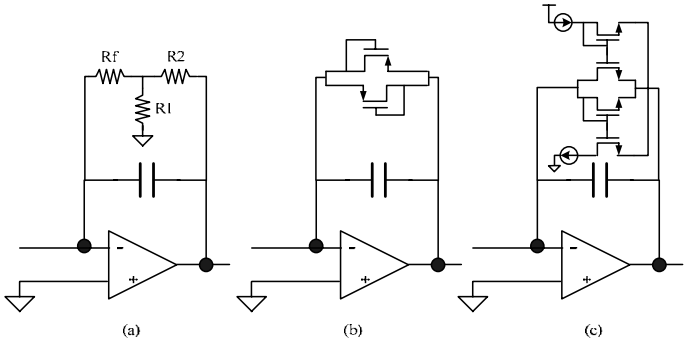

Figure 15. Charge Amplifier Feedback

The digital signal processing path is illustrated in Fig. 16, which includes phase adjustments, decimation filters, FIR filters and synchronous demodulation.

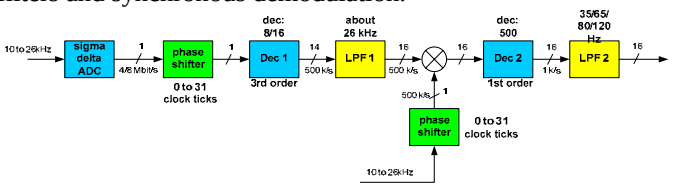

Figure 16. Digital Signal Processing Path

TEST RESULTS AND DSICUSSION

By virtue of having an analog output channel, a digital SPI output data bus, and two available analog input channels, the MicroGyro is capable of operating in many system configurations, from stand-alone rate sensors with or without external input analog signals (e.g. accelerometers) to multi-axis sensor configurations. This produces an automotive MEMS gyro in a single SMT package with exceptional performance, extensive self-monitoring, low cost and adaptability to the most performance applications, including ESC and rollover airbag deployment, as well as Low Drift/Lane Keeping applications. The test results of the MicroGyro are presented and discussed in the following.

Turn On Performance

Fig. 17 shows the test results of turn on. The red curve, I/V converter output, shows the buildup of the energy in the fork. The blue curve is the drive voltage. At startup, the drive voltage is at rail to drive the fork very hard , consequently reducing the startup time. When the AGC loop is servoed the drive voltage magnitude is controlled by the AGC loop. Fig. 18 shows that the MicroGyro has a reliable turn on performance with nominal turn on time of within 800mS.

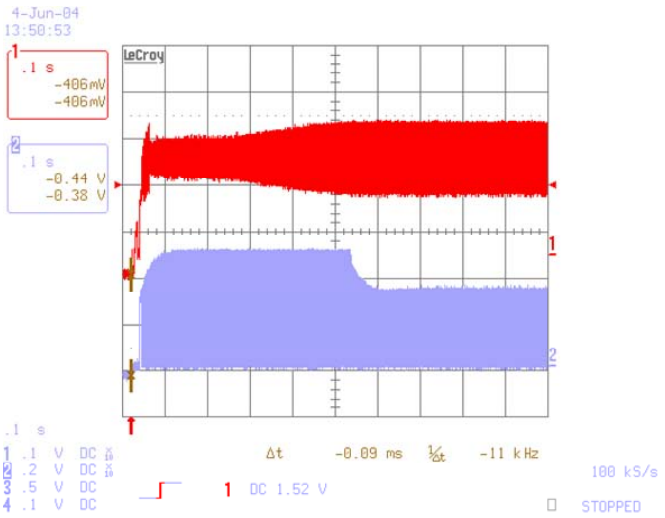

Figure 15. Oscillation Startup Characerization

Figure 17. MicroGyro Turn On Characerization

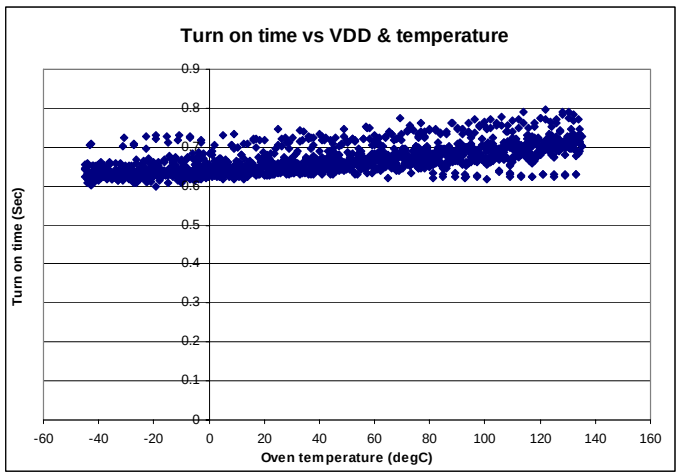

Figure 18. Turn On Time vs Temperature and Power Supply

Rate Range Capability

The angular rate range capability covers every conceivable automotive gyro class with a performance exceeding ±800°/s with a nearly immeasurable linearity error.

It is believed that this large range capability is a first for an automotive MEMS gyro. Systron Donner's only experience with gyros having this large range is in the aerospace missile market. Fig. 19 illustrates the rate range capability at a worst case temperature of 125°C. It robustly operates until saturation at ±819°/s, greatly exceeding the ±300°/s rate range requirement for rollover airbag deployment applications. In addition, the analog rate output saturates gracefully and recovers well for over-range input rates. The digital output simply saturates at the full scale output.

While the analog rate output of the MicroGyro is scaled to full voltage range for the selected rate range, the digital SPI output retains the same least significant bit (LSB) weighting for rate regardless of selected rate range. Consequently, the digital output has a resolution of 0.025°/s/bit for the full rate range up to ±819°/s.

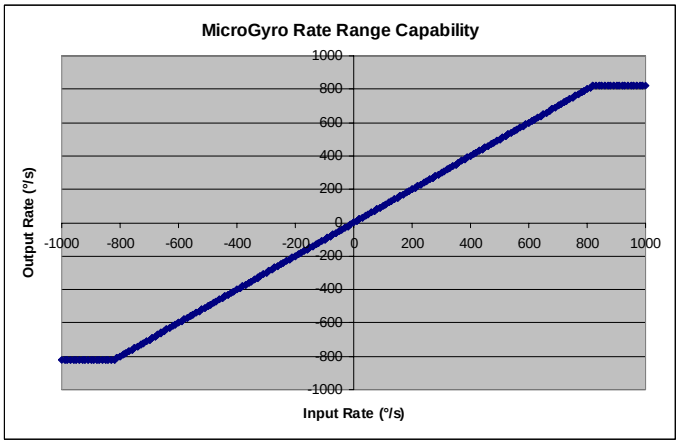

Figure 19. MicroGyro Rate Range Capability

Scale Factor Linearity

The scale factor (sensitivity) linearity specification of <±0.5°/s highlights another traditional strength of the QRS gyro. While scale factor is routinely factory calibrated, it has never been necessary to calibrate over temperature. Ambient temperature calibration is adequate. The MicroGyro continues this desirable feature and avoids the need to submit production gyros to simultaneous (and inconvenient) rate and temperature environments. In Fig. 20 linearity residual errors over the full rate range of ±819°/s are shown to be a very small fraction of the specification requirement.

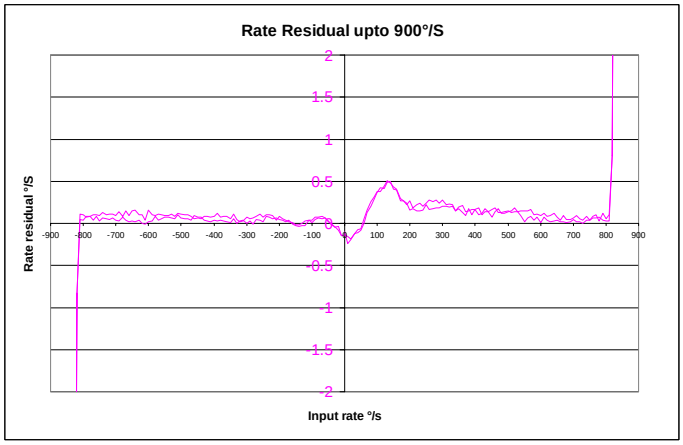

Figure 20. MicroGyro Scale Factor Linearity

Historically, scale factor linearity has always been a robust parameter for Systron Donner's gyros. Therefore, no comparison data from previous generation gyros is included for comparison.

Sensitivity Over Temperature

A difficult performance specification for many MEMS gyros to meet robustly is scale factor (sensitivity) over temperature. With the 40°C to +125°C "under the hood"

requirement for the MicroGyro, the challenge is even more severe. An advantage of the QRS technology is the excellent linearity and temperature stability of the basic tuning fork sensing element, as well as the signal conditioning electronics which robustly meet the requirement of ±2 percent scale factor error over temperature as shown in Fig. 21.

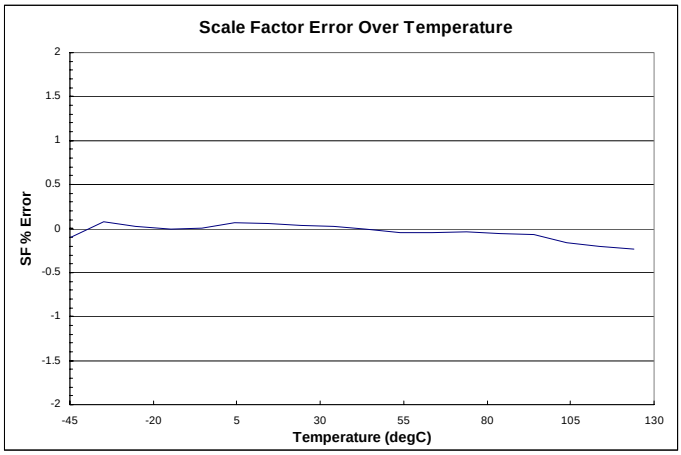

Figure 21. MicroGyro Sensitivity vs Temperature

Noise Performance

Another typical strength of QRS technology gyros has been relatively low noise characteristics. A common automotive noise requirement is 0.5°/s/rtHz. The robustly exceeds this requirement by about sixteen to one by exhibiting a typical output noise performance of less than 0.03°/s/rtHz.

Bias Over Temperature

The most significant challenge for most MEMS gyros is the ability to meet zero rate bias offset over temperature. The superior stability of quartz, attention to spurious resonant mode location, combined with a robust signal processing and temperature compensation scheme provide bias over temperature performance exceeding all automotive requirements. At an early stage of development, the exhibited less than ±0.5°/s bias over temperature for 95 percent of all units manufactured. Long-term stability has also been demonstrated with over 1000 hours of accelerated life test at 125°C. Fig. 22 illustrates typical bias over the under the hood" temperature range of -40°C to +125°C displayed against the ESC specification of ±2°/s.

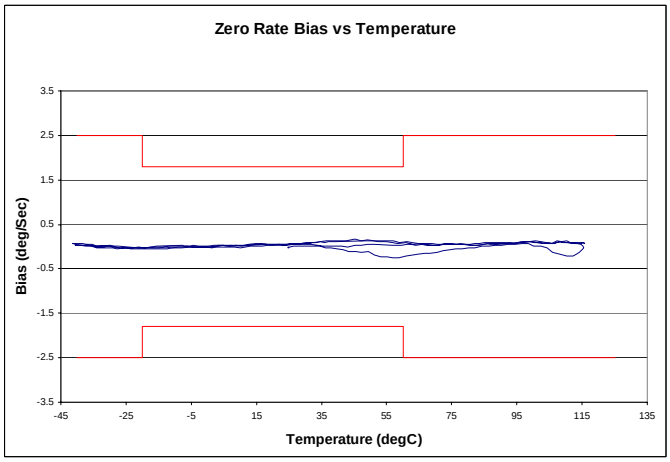

Figure 22. MicroGyro Zero Rate Bias vs. Temperature

Finally, this MicroGyro has exceptional ability to continuously self-monitor for gyro defects during vehicle operation. The MicroGyro supplements this with an extremely thorough manufacturing test at the component and completed assembly level. The comprehensive fault coverage includes all functional blocks in the ASIC, as well as the fork drive and pick-up tines. At this writing, final results are not available, but early estimate shows over 85 percent of all faults are detectable.

CONCLUSION

Systron Donner's MicroGyro has achieved 0.025°/s/LSB resolution in the digital SPI rate output, and a low noise floor of 0.03°/s/rtHz with full rate range of ±819°/s up to bandwidth of 120Hz.

REFERENCES

1. W.A. Clark, R.T. Howe, and R. Horowitz, "Surface Micromachined Z-Axis Vibratory Rate Gyroscope," Solid-State Sensor and Actuator Workshop, HiltonHead Island, SC, June 1996, p.283-287

2. Xuesong Jiang, Joseph I. Seeger, Michael Kraft, and Bernhard E. Boser, "A Monolithic Surface Micromachined Z-Axis Gyroscope with Digital Output," Symp. on VLSI Circuits Dig. of Tech. Papers, June 2000

3. Xuesong Jiang, Sunil A. Bhave, Joseph I. Seeger, Roger, T. Howe, Bernhard E. Boser, "ΣΔ Capacitive Interface for a Vertically-Driven X&Y-Axis Rate Gyroscope," ESSCIRC 2002, p.639-642

4. Jan Söderkvist, "A mathematical analysis of flexural vibrations of piezoelectric beams with applications to angular rate sensors", doctoral dissertation at Uppsala University, 1990

5. Asad M. Madni, Lynn E. Costlow, "Common Design Techniques for Quartz Rate Sensors for Both Automotive and Aerospace/Defense Market Applications", Proceedings of IEEE Sensors, 2002, vol. 2, p. 1597-1602